

# EIT-based photonic memory with near-unity storage efficiency

Ya-Fen Hsiao<sup>1,2</sup>, Pin-Ju Tsai<sup>1,3</sup>, Hung-Shiue Chen<sup>1</sup>, Sheng-Xiang Lin<sup>1,3</sup>, Chih-Chiao Hung<sup>1</sup>, Chih-Hsi Lee<sup>1</sup>, Yi-Hsin Chen<sup>4</sup>, Yong-Fan Chen<sup>5</sup>, Ite A. Yu<sup>4,\*</sup>, and Ying-Cheng Chen<sup>1,\*</sup>

<sup>1</sup>*Institute of Atomic and Molecular Sciences, Academia Sinica, Taipei 10617, Taiwan*

<sup>2</sup>*Molecular Science and Technology Program, Taiwan International Graduate Program, Academia Sinica and National Central University, Taiwan*

<sup>3</sup>*Department of Physics, National Taiwan University, Taipei 10617, Taiwan*

<sup>4</sup>*Department of Physics, National Tsing Hua University, Hsinchu 30043, Taiwan*

<sup>5</sup>*Department of Physics, National Cheng Kung University, Tainan 70101, Taiwan*

(Dated: January 24, 2019)

Quantum memory is an important component in the long-distance quantum communication system based on the quantum repeater protocol. To outperform the direct transmission of photons with quantum repeaters, it is crucial to develop quantum memories with high fidelity, high efficiency and a long storage time. Here, we achieve a storage efficiency of 96% for a photonic memory based on the electromagnetically induced transparency (EIT) scheme in cold atomic media with an optical depth of near 1000. At a storage efficiency of 50%, we also obtain a fractional delay of 1200. Both are the best record to date in all kinds of the schemes for the realization of quantum memory. Our work significantly advances the pursuit of a high-performance photonic memory and should have important applications in quantum information science.

Quantum memory is a device that can store and then retrieve a quantum state on demand[1]. It is an important building block in the development of quantum communication[1–3] and quantum computation[4]. Parameters for evaluating the performance of a quantum memory include the fidelity, efficiency, storage time, and capacity[1]. In the past few years, significant progress has been made in improving many of the performance parameters[5–10]. Highly efficient quantum memory is enormously important for the realization of quantum repeater. For example, an increase of 1% in efficiency may decrease the entanglement distribution time by 7-18%, depending on the protocol. It is crucial to achieve an efficiency of  $\geq 90\%$  to find regimes that quantum repeaters perform better than direct transmission[1, 3].

The memory efficiency is determined both by technical loss and the storage efficiency (SE), defined by the ratio of the storage-and-retrieval output to the input pulse energies. The SE evaluates the intrinsic efficiency of a memory, which depends on the storage mechanism and the media properties. Quantum memories have been implemented based on a variety of mechanisms including the off-resonant Raman interactions[10], atomic frequency combs (AFC)[11], gradient echo[6], and electromagnetically induced transparency (EIT)[12]. The best achieved SE of 87% is based on the gradient echo[6]. For the other methods, the best recorded SE is 35% obtained using the AFC[13], 43% using the Raman interaction[10], and 78% using the EIT[14–19].

A high optical depth (OD, denoted as  $D$ ) for the media is the ultimate requirement to obtain a high SE in EIT-based memory[20, 21]. In addition, a low decoherence rate for the long-lived atomic states is another crucial requirement[18]. However, at high ODs, some nonlinear optical effects may become significant to induce complications to the quantum memory. For exam-

ple, the off-resonant excitation of the control field on the nearby transition or the probe transition can induce photon switching[22, 23] or four-wave mixing (FWM)[25–28] effect which may lead to degradation in the SE and/or fidelity[27]. Thus, proper choice of the energy level scheme to minimize these effects is also crucial.

Our experiment fulfills all these requirements and allows us to obtain a SE of 96%. This SE is not only the best record to date in all kinds of memory schemes, but also a milestone for the development of quantum repeaters to outperform the direct transmission. We also achieved a record-high fractional delay (FD) of 1200 at 50% SE. This parameter is an important figure of merit for quantum memory applications. It evaluates how many qubit operations that a memory can provide. We also point out a strategy to increase this FD by more than a factor of 10 with a shorter probe pulse and a higher control intensity.

EIT-based quantum memory relies on the slow light effect or the dark-state polariton which is a coherent superposition of the probe optical field and the collective atomic coherence. By adiabatically ramping the control field off and on, one can coherently convert the probe field into collective atomic excitation and store it inside the media until being retrieved as an optical field[12]. The overall SE  $\eta$  depends on three factors, denoted as  $\eta_{tran}$ ,  $\eta_{comp}$  and  $\eta_{stored}$ , such that  $\eta = \eta_{tran}\eta_{comp}\eta_{stored}$ .  $\eta_{tran}$  is the transmission efficiency of a slow light pulse.  $\eta_{comp}$  indicates the fraction of a probe pulse that are compressed into the medium during storing.  $\eta_{stored}$  indicates the remaining efficiency after a given storage time. For a large enough OD (e.g.  $\geq 100$ , see[29]) and a short storage time, both  $\eta_{comp}$  and  $\eta_{stored}$  can be close to one and  $\eta_{tran}$  dominates the SE.

An analysis of the slow light propagation in an EIT medium by the Maxwell-Bloch equations shows that the

transmission of a Gaussian probe pulse with an intensity FWHM width of  $T_p$  is [29, 30],

$$\eta_{tran} = \frac{e^{-2\gamma T_d}}{\sqrt{1 + 32 \ln 2 \frac{\gamma_{31}^2 \zeta^2}{\Gamma D}}} = \frac{e^{-2\gamma T_d}}{\sqrt{1 + \left(\frac{4 \ln 2}{T_p \Delta \omega_{EIT}}\right)^2}}, \quad (1)$$

where  $\Delta \omega_{EIT} = \sqrt{\frac{\ln 2}{2}} \frac{\Omega_c^2}{\sqrt{D} \gamma_{31} \Gamma}$  is the FWHM EIT bandwidth,  $\Omega_c$  is the Rabi frequency of the control field,  $T_d$  is the group delay,  $\zeta = \frac{T_d}{T_p}$ ,  $\gamma$  is the ground-state decoherence rate,  $\gamma_{31}$  is the decay rate of the optical coherence  $\rho_{31}$ , and  $\Gamma$  is the spontaneous decay rate, which is  $2\pi \times 4.575$  MHz for cesium  $6P_{1/2}$  state and  $2\pi \times 5.234$  MHz for the  $6P_{3/2}$  state[31]. The numerator and denominator in Eq.(1) indicates that  $\eta_{tran}$  is limited by the finite ground-state decoherence rate and the finite EIT bandwidth. A small  $\gamma$  and a large OD are two key parameters to obtain a high SE at a fixed  $\zeta$ . To keep  $\zeta$  fixed at a given  $T_p$  for a larger OD, one has to increase the control intensity because  $T_d \cong \frac{D\Gamma}{\Omega_c^2}$ . In the ideal case with  $\gamma = 0$  and  $\gamma_{31} = \Gamma/2$ , the transmission approaches unity with the scaling law  $\eta_{tran} = 1 - \frac{40}{D}$ . We assume  $\zeta = 2.7$  such that  $\eta_{comp} > 0.99$ . In Refs.[20, 21], the authors describe an optimal method in which the probe waveform is optimized to maximize the SE for a given OD. Compared to the case of a Gaussian waveform, this method gains a significant improvement in SE at moderate ODs. At high ODs, the SE obtained with optimal waveform does not deviate too much from that obtained with a Gaussian waveform. A scaling law of  $\eta = 1 - \frac{38}{D}$  for the optimal method was derived[21].

We implemented the EIT-based photonic memory with both cesium  $D_2$  and  $D_1$  lines with the level scheme shown in Fig.1 (a) and (b). The population is prepared in the single Zeeman state by the optical pumping method[32]. With  $\sigma^+$ -polarized control and probe fields, the EIT system involves only three Zeeman sub-levels in both schemes. However, the control field can off-resonantly couple to the nearby  $|2\rangle \rightarrow |4\rangle$  transition in the  $D_2$  scheme. This coupling induces an additional channel for multiphoton loss[18] and causes the N-type photon switching effect[22, 23]. It introduces a control-intensity-dependent decay rate for the ground-state coherence and limits the SE at high ODs[18].

To illustrate this effect, we take EIT spectra for various control intensities at a given OD for both schemes. A significant difference in the degree of transparency at EIT resonances is observed between the two schemes[29]. The transparency is only up to 70% for the  $D_2$  scheme while it is almost 100% for the  $D_1$  scheme. By fitting the spectra to the corresponding lineshapes, the parameters  $\gamma$ ,  $D$ ,  $\Omega_c$  can be obtained[29]. Fig. 2(a) depicts  $\gamma$  versus the control power for both schemes. As expected,  $\gamma$  for the  $D_2$  scheme are much larger than those of  $D_1$  scheme and scale linearly with the control power. As shown in[29], the off-resonant coupling of the control field introduces an effective ground-state decoherence rate as

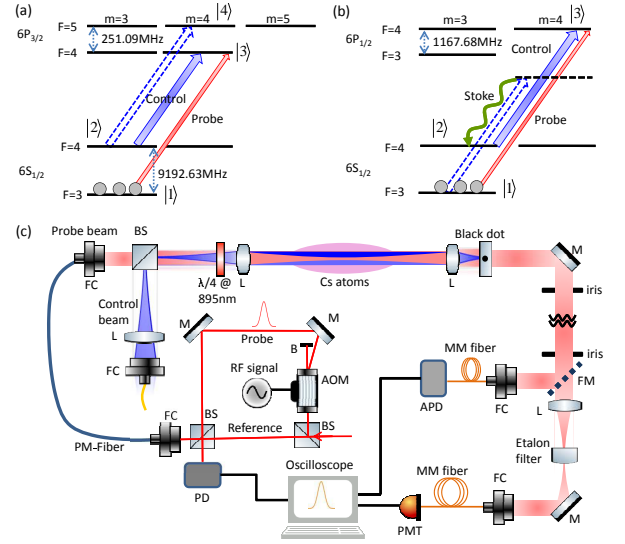


FIG. 1: (a) and (b): Relevant energy levels and laser excitations for the  $D_2$  and  $D_1$  EIT scheme, respectively. In  $D_2$  scheme, the control field off-resonantly excites the  $|2\rangle \rightarrow |4\rangle$  transition, and induce the N-type photon switching effect. In  $D_1$  scheme, the control field off-resonantly excites the probe transition and acts as a pumping field to induce a FWM process, which leads to the Stoke generation and a probe gain. (c) Schematic experimental setup. AOM: acousto-optic modulator; APD: avalanche photodetector; B: block; BS: beam splitter; FC: fiber coupler; FM: flip mirror; L: lens; M: mirror; MM fiber: multimode fiber; PD: photodetector; PM fiber: polarization-maintaining fiber; PMT: photomultiplier tube.

$\frac{(\epsilon \Omega_c)^2}{4\delta_s^2} \gamma_{41}$ , where  $\epsilon = \sqrt{48/7}$  is the ratio of the Clebsch-Gordon coefficient for the  $|2\rangle \rightarrow |4\rangle$  to that of the control transition and  $\delta_s = 2\pi \times 251.0916$  MHz. Instead, the  $D_1$  EIT scheme is an ideal three-level system free from the photon switching effect. Therefore, we focus our study on the  $D_1$  scheme. The off-resonant coupling of the control field also causes the EIT resonant frequency shifts due to the ac Stark shifts, as shown in Fig. 2(b).

We utilize a magneto-optical trap (MOT) of cesium in addition to many techniques to obtain cold atomic medium with ODs up to 1000[32]. Efforts are made in obtaining a good mutual coherence between the control and probe lasers and a reduction of the dc and ac stray magnetic fields to obtain a  $\gamma$  of a few  $10^{-4}\Gamma$ . To reduce  $\gamma$  to  $10^{-4}\Gamma$  level due to atomic motion[33, 34], the control and probe beams are copropagating with an angle  $\theta$  of  $< 1^\circ$ . Under such a condition, leakage of the control light into the detector for probe detection becomes an issue. As shown in Fig. 1(c), a series of arrangements including a window with a black dot, some irises, an etalon filter (Quantaser FPE001) and a multimode fiber are used to obtain a 73 dB isolation of the control power. We have to point out that due to the dispersive (focusing or defocusing) effect of the atomic clouds, these filtering optics might lead to problems in the measurement of SE if not carried out carefully[35]. Optimization of the filtering op-

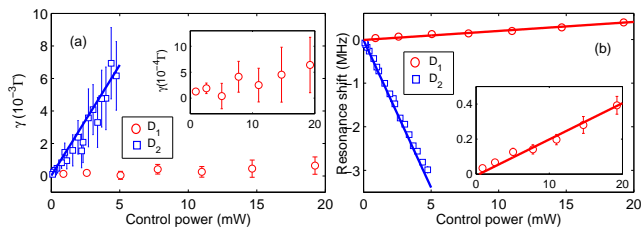


FIG. 2: (a)  $\gamma$  and (b) EIT resonant frequency shift versus the control power for both  $D_1$  and  $D_2$  EIT schemes. In (a), the blue line is a calculation with  $\gamma = \gamma_0 + \frac{(\sqrt{48/7}\Omega_c)^2}{4\delta_s^2}\gamma_{41}$ , where  $\gamma_0 = 0.0001\Gamma$ ,  $\gamma_{41} = 0.7\Gamma$ . In (b), the red line is a calculation of the ac Stark shifts of state  $|1\rangle$  ( $\frac{(\sqrt{7}\Omega_c)^2}{4\delta_{hf}}$ ) in the  $D_1$  scheme, where  $\delta_{hf} = 2\pi \times 9.1926$  GHz. The factor  $\sqrt{7}$  is the ratio of the Clebsch-Gordan coefficient between the probe and control transition. The blue line is a calculation of the difference of the ac Stark shifts between states  $|1\rangle$  and  $|2\rangle$  in the  $D_2$  scheme, which is  $\frac{(\sqrt{25/7}\Omega_c)^2}{4\delta_{hf}} - \frac{(\sqrt{48/7}\Omega_c)^2}{4\delta_s}$ , where  $\sqrt{25/7}(\sqrt{48/7})$  is the ratio of the Clebsch-Gordan coefficient of the probe ( $|2\rangle \rightarrow |4\rangle$ ) to that of the control transition.

tics and precise determination of EIT resonance by phase measurement using a beatnote interferometer[36, 37] are keys for a reliable measurement of SE[29].

Fig. 3(a) depicts a representative EIT spectrum of the  $D_1$  scheme. The red line in Fig. 3(a) is a fitting curve of the EIT lineshape  $T(\delta_p) = \exp\left\{\frac{D\Gamma}{2} \text{Re}\left(\frac{i(\delta_p - \delta_c) - \gamma}{(i\delta_p - \gamma_{31})(i(\delta_p - \delta_c) - \gamma) + \frac{\Omega_c^2}{4}}\right)\right\}$ , where  $\text{Re}()$  stands for the real part of the expression inside the bracket[32]. In this case, the fitting parameters  $\{D, \Omega_c, \gamma, \delta_c\}$  are  $\{942(90), 6.33(12)\Gamma, 0.0001(1)\Gamma, -0.019(6)\Gamma\}$ , respectively. The quantities shown in the brackets are the  $2\sigma$  standard deviations. The decoherence rate  $\gamma_{31}$  is set to  $0.6\Gamma$ . It is larger than the ideal case of  $0.5\Gamma$  due to the finite laser linewidth and frequency fluctuation. More discussions on this issue are in[29].

Fig. 3(b) depicts one representative dataset of the input, slow and stored-and-retrieved probe pulses. This dataset is corresponding to the data point with the largest OD in Fig. 4(b). The efficiency of the retrieved pulse is 95.9(1.0)%. It is the largest SE we have achieved. The purple line in Fig. 3(b) is a calculation of slow light with parameters  $\{D, \Omega_c, \gamma, \gamma_{31}\}$  of  $\{946, 7.7\Gamma, 0.0001\Gamma, 0.6\Gamma\}$ , respectively.

Fig. 3(c) depicts the representative beatnote data for the input, slow, and stored-and-retrieved pulses. Fig. 3(d)-(e) show parts (50 ns duration) of the beatnote data around the peaks of the three traces, respectively. It is evident that the phase coherence is preserved for both the slow and retrieved pulses. Quantitatively, the classical fidelities which characterize the resemblance of the electric field of the slow or retrieved pulse to the input one are 98.1% and 93.1%, respectively[18, 38].

From Eq.(1), it is evident that if one keeps  $\zeta = \frac{T_d}{T_p}$  as a constant for a given  $D$ , then the denominator is

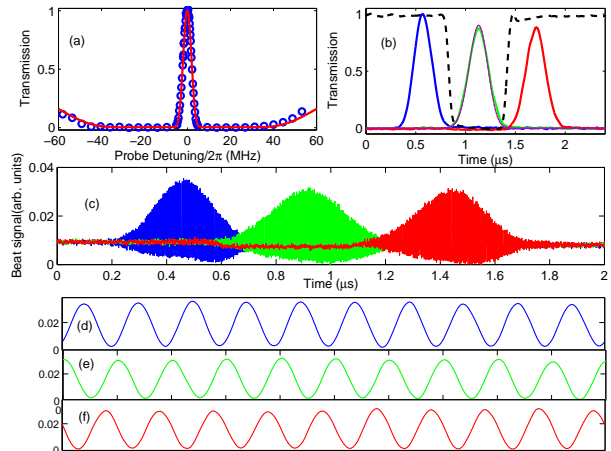


FIG. 3: (a) A representative EIT spectrum. The red line in a fitting curve with fitting function and fitting parameters mentioned in the main contexts. (b) Blue, green and red traces are the input, slow, and stored and retrieval pulse, respectively. The dashed black trace is the control intensity. The efficiencies for the slow and retrieved pulse are 96.2(1.3)% and 95.9(1.0)%, respectively. The purple line is a calculated slow light curve with parameters  $\{D, \Omega_c, \gamma, \gamma_{31}\}$  of  $\{946, 7.7\Gamma, 0.0001\Gamma, 0.6\Gamma\}$ , respectively. (c) A representative beatnote data. The parameters  $\{D, \Omega_c\}$  are  $\{360, 4.6\Gamma\}$ , respectively. (d),(e),(f) Parts of the beatnote data (50ns duration) around the peaks of the three pulses in (c).

a constant and the numerator exponentially approaches 1 when  $T_p$  is approaching zero because  $T_d = \zeta T_p$ . Thus, one gains the SE for a shorter  $T_p$ . To keep  $\zeta$  constant when decreasing  $T_p$ , one has to increase the control intensity since  $T_d = \frac{D\Gamma}{\Omega_c^2}$ . Experimentally, one is limited by the available control power when shortening  $T_p \rightarrow 0$ . We choose the shortest  $T_p$  of  $\sim 200$  ns which is limited by the manageable control power at the largest OD. Fig. 4(a) depicts SE versus  $T_p$  for a fixed OD of 340 with  $\zeta = 2.4 \pm 0.05$ . The calculation (black line) with Eq.(1) and  $\gamma = 0.0001\Gamma$  fits the data very well.

Next, we address the SE versus storage time. A long storage time is advantageous for quantum memory applications. For the MOT setup, it is limited to a  $\sim 1$  ms by atomic motion, because atoms are not trapped during the storage period. Reduction of the stray magnetic field and a small  $\theta$  are two keys to prolonging the storage time[33]. We minimize the stray magnetic field via iteratively fine tuning the compensating magnetic fields to maximize the transmission of the retrieved pulse and then increasing the storage time and repeating the optimization[39]. Fig. 4(b) shows an example of SE versus the storage time with an OD of 420 and  $\theta = 0.5^\circ$ . The FD at 50% SE is 1200, which is the largest record to date[6].

The FD at 50% SE can be even larger if  $T_p$  is shorter and the control intensity is higher to keep  $\zeta$  fixed. Since the decoherence rate  $\gamma$  due to the off-resonant excitation of the control field is  $\propto \Omega_c^2$ , one concern is that  $\eta_{tran}$  may significantly reduce at high control intensity. For a

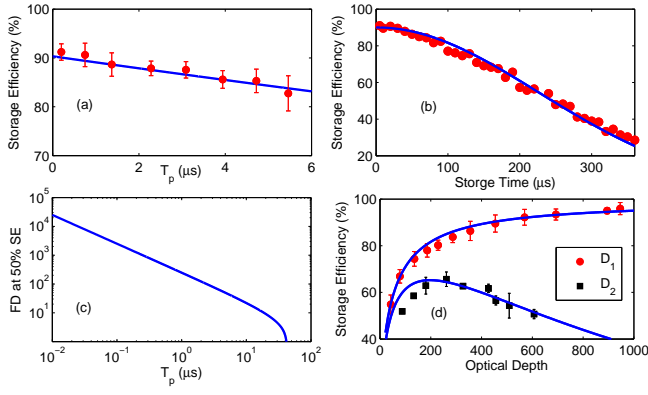


FIG. 4: (a) SE versus  $T_p$  for the  $D_1$  scheme. The blue line is a calculation of Eq. (1) with parameters  $\{\zeta, \gamma_{31}, \gamma\}$  of  $\{2.4, 0.6\Gamma, 0.0001\Gamma\}$ , respectively. (b) SE versus storage time. The black line is a fit curve, which is  $90\exp(-t^2/\tau^2)$  with  $\tau = 325\mu\text{s}$ . (c) FD at 50% SE for the results in (a) and the storage time of (b). (d) SE versus OD for the  $D_1$  (red circle) and  $D_2$  (blue square) schemes. The red line is a calculation based on Eq.(1) for the  $D_1$  scheme with parameters  $\{T_p, \zeta, \gamma_{31}, \gamma\}$  of  $\{207 \text{ ns}, 2.7, 0.6\Gamma, 0.0001\Gamma\}$ , respectively. The blue line is a calculation of Eq.(1) for the  $D_2$  scheme with parameters  $\{T_p, \zeta, \gamma_{31}\}$  of  $\{207 \text{ ns}, 2.7, 0.7\Gamma\}$  and  $\gamma = \gamma_0 + \frac{(48/7)\Omega_c^2}{4\delta^2}\gamma_{41}$ , where  $\gamma_0 = 0.0005\Gamma$ ,  $\gamma_{31} = \gamma_{41} = 0.7\Gamma$ .

fixed OD and  $\zeta$ , the denominator of Eq.(1) is fixed. The numerator of Eq.(1) ( $\exp(-2\gamma\zeta T_p)$ ) is independent of the control intensity since if  $T_p$  decreases by a factor then  $\gamma$  will increase by the same factor and both cancel out. In Fig. 4(c), we plot the expected FD at 50% SE with the results of Fig. 4(a) and an coherence time  $\tau$  of 325  $\mu\text{s}$ . With an OD of 1000 and  $T_p=10$  ns, the required  $\Omega_c$  is  $34\Gamma$ . The FD increases by more than a factor of 10.

Fig. 4(d) depicts the SE versus OD for the  $D_1$  system(circle). We keep  $\zeta$  as a constant( $\sim 2.7 \pm 0.05$ ) for all ODs by varying the control intensity. The red line is a calculation of Eq.(1) with  $\gamma = 0.0001\Gamma$  and  $\gamma_{31} = 0.6\Gamma$ . From Eq.(1), it is evident that the SE approaches an asymptote value of  $\exp(-2\gamma T_d)$  in the high OD limit. Quantitatively, if  $\gamma$  increases from  $10^{-4}\Gamma$  by a factor of 10 or 100 with  $T_p = 200\text{ns}$ , the asymptotic SE decreases from 99.4% to 94.0% or 53.9%, respectively. This highlights the importance to achieve a low  $\gamma$  in obtaining a high SE. For comparison, the SE versus OD data for the  $D_2$  scheme are also shown(rectangle). The SE peaks at 65% at an OD around 262 and goes down at larger ODs. The calculation based on Eq.(1) with a control-intensity-dependent decoherence rate agrees well with the data[29].

In the level scheme depicted in Fig.1(b), the off-resonant coupling of the control field on the probe transition can act as a pumping field to induce a FWM process[25, 26]. The FWM generates the Stokes photons and induces a probe gain. The classical behaviors of the FWM have been well studied[24–26]. Its effect in the quantum regime has been studied theoretically[27] and partially tested[40]. The quantum noise photon due

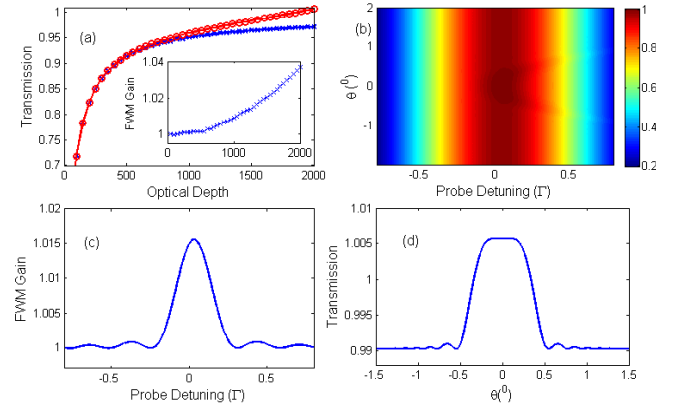


FIG. 5: (a) Numerical calculations of  $\eta_{tran}$  versus OD with (red) and without (blue) the presence of FWM. Perfect phase matching is assumed and  $T_p$  is 200 ns.  $\Omega_c$  is adjusted for each OD to keep  $\zeta=2.7$ . Inset shows the ratio of those two traces, reflecting the FWM gain versus OD. The results in (b)-(d) are based on the steady-state calculation including the phase mismatching. (b) Contour plot of the probe transmission versus  $\theta$  and  $\delta_p$ . The parameters  $\{D, \Omega_c, \gamma\}$  are  $\{1000, 6.72\Gamma, 0.0002\Gamma\}$ , respectively. (c) Ratio of probe transmission for  $\theta = 0^\circ$  to that of  $\theta = 2^\circ$  versus  $\delta_p$ . At  $\theta = 2^\circ$ , the effect of FWM is negligible. This curve reflects the FWM gain versus  $\delta_p$ . (d) Probe transmission versus  $\theta$  for  $\delta_p = 0.04\Gamma$ .

to FWM is detrimental to the quantum memory application. The noise photon exponentially grows with the parameter  $x = D\Gamma/\delta_{hf}$ . To reduce the FWM, it is better to choose an energy level scheme which has a larger  $\delta_{hf}/\Gamma$ [27]. Among the stable alkali, cesium has the most favorable value ( $\sim 2009$ ) due to its largest hyperfine splitting and the relatively small  $\Gamma$ .

To evaluate the FWM effect, we perform a semiclassical calculation of the probe gain[26, 29] including the phase mismatching[24, 28]. A larger gain indicates a more reduction of the fidelity[27]. Fig. 5(a) depicts the numerical calculation of the transmission versus OD for a probe pulse of  $T_p=200$  ns and  $\zeta=2.7$  under the perfect phase matching condition. The red and blue traces indicate the transmission with and without the presence of FWM. Inset shows the ratio of the two traces, indicating the FWM gain versus OD. Even at an OD of 1000, the gain is only up to 0.9%, which is about our experimental uncertainty of  $\sim \pm 1\%$  for the SE measurement.

Fig.5(b) depicts a calculated contour plot of the probe transmission versus  $\delta_p$  and  $\theta$  in the steady state for  $D=1000$ ,  $\Omega_c = 6.72\Gamma$  and  $\gamma = 0.0002\Gamma$ . The maximum FWM gain ( $\sim 1.5\%$ ) occurs at  $\delta_p = 0.04\Gamma$  due to the ac Stark shift introduced by the control field driving on the probe transition, as shown in Fig. 5(c). Fig. 5(d) depicts the probe transmission versus  $\theta$  for  $\delta_p = 0.04\Gamma$ . For  $\theta \geq 0.5^\circ$ , the FWM can be greatly suppressed, because the phase matching condition is not satisfied. Therefore, it is possible to obtain a high SE with a negligible FWM effect even with an OD of 1000.

However, there is a tradeoff between breaking the

phase matching condition and obtaining a long storage time, because the former requires a larger  $\theta$  while the later requires a smaller  $\theta$ . This contradiction could be remedied if the cold atoms were trapped by an dipole trap[41] or optical lattices[7] with an even colder temperature since one can choose a relatively large  $\theta$  but still enjoy a long storage time. One more advantage with such setups and arrangement would be a lower technical loss without using the filtering optics. In our setup, the overall collection efficiency of the filtering optics is 31%.

In conclusion, we demonstrate that it is feasible to achieve a storage efficiency of approaching unity with a negligible FWM effect for an EIT-based photonic memory. Although only weak coherent state are used at this moment, we expect the results can be applied to the quantum state of light as well[17].

This work was supported by the Ministry of Science and Technology of Taiwan under grant numbers 103-2119-M-001-012 and 103-2112-M-001-010-MY3. This work was done under a collaboration project (Science Vanguard Research Program of MOST) with I.A.Y. as the project leader and Y-C.C. and Y-F.C. as the subproject leaders. Correspondence of the project contents can be addressed to I.A.Y. Correspondence and requests for materials of this work can be addressed to Y-C.C. We also acknowledge the support from NCTS of Taiwan.

---

\* Electronic address: [yu@phys.nthu.edu.tw](mailto:yu@phys.nthu.edu.tw); [chenyc@pub.iams.sinica.edu.tw](mailto:chenyc@pub.iams.sinica.edu.tw)

- [1] F. Bussi eres, N. Sangouard, M. Afzelius, H. de Riedmatten, C. Simon, and W. Tittel, *J. Mod. Opt.* **60**, 1519(2013)
- [2] Duan, L. M., Lukin, M. D., Cirac, J. I. and Zoller, P. *Nature* **414**, 413-418 (2001).
- [3] N. Sangouard, C. Simon, H. de Riedmatten, and N. Gisin. *Rev. Mod. Phys.* **83**, 33(2011).
- [4] P. Kok, W. J. Munro, K. Nemoto, T. C. Ralph, J. P. Dowling, and G. J. Milburn. *Rev. Mod. Phys.* **79**, 135(2007).
- [5] Z.-Q. Zhou, W.-B. Lin, M. Yang, C.-F. Li, and G.-C. Guo. *Phys. Rev. Lett.* **108**, 190505(2012).
- [6] Y.-W. Cho, T. Campbell, J. L. Evertt, J. Bernu, D. B. Higginbottom, M. T. Cao, J. Geng, N. P. Robins, P. K. Lam, and B. C. Buchler, *Optica* **3**,, 100(2016).
- [7] Y. O. Dudin, L. Li, and A. Kuzmich. *Phys. Rev. A* **87**, 031801(R)(2013).
- [8] G. Heinze, C. Hubrich, and T. Halfmann. *Phys. Rev. Lett.* **111**, 033601(2013).
- [9] D.-S. Ding, Z.-Y. Zhou, B.-S. Shi, and G.-C. Guo. *Nat. Commun.* **4**, 1(2013).
- [10] K. F. Reim, J. Nunn, V. O. Lorenz, B. J. Sussman, K. C. Lee, N. K. Langford, D. Jaksch, and I. A. Walmsley. *Nat. Photon.* **4**, 218(2010).
- [11] M. Afzelius, C. Simon, H. de Riedmatten, and N. Gisin. *Phys. Rev. A* **79**, 052329(2009).
- [12] M. Fleischhauer and M. D. Lukin. *Phys. Rev. Lett.* **84**, 5094-5097(2000).
- [13] A. Amari, A. Walther, M. Sabooni, M. Huang, S. Kr oll, M. Afzelius, I. Usmani, B. Lauritzen, N. Sangouard, and H. de Riedmatten, *J. Lumin. J. of Lumine.* **130**, 1579(2010).
- [14] I. Novikova, A.V. Gorshkov, D. F. Phillips, A. S. Sorensen, M. D. Lukin, and R. L. Walsworth. *Phys. Rev. Lett.* **98**,243602 (2007).
- [15] N. B. Phillips, A.V. Gorshkov, and I. Novikova. *Phys. Rev. A* **78**, 023801 (2008).
- [16] S. Zhang, S. Zhou, M. M. T. Loy, G.K. L. Wong, and S. Du. *Opt. Lett.* **36**, 4530 (2011).
- [17] S. Zhou, S. Zhang, C. Liu, J. F. Chen, M. M. T. Loy, G. K. L. Wong, and S. Du. *Opt. Express.* **20**, 24124(2012).
- [18] Y.-H. Chen, M.-J. Lee, I.-C. Wang, S. Du, Y.-F. Chen, Y.-C. Chen, and I. A. Yu. *Phys. Rev. Lett.* **110**, 083601(2013).
- [19] D. Schraft, M. Hain, N. Lorenz, and T. Halfmann. *Phys. Rev. Lett.* **116**, 073602(2016).
- [20] A. V. Gorshkov, A. Andr e, M. Fleischhauer, A. S. Sorensen, and M. D. Lukin. *Phys. Rev. Lett.* **98**, 123601(2007).
- [21] A. V. Gorshkov, A. Andr e, M. D. Lukin, and A. S. Sorensen. *Phys. Rev. A* **76**, 033805(2007).
- [22] H. Schmidt and A. Imamoglu. *Opt. Lett.* **21**, 1936 (1996).
- [23] S. E. Harris and Y. Yamamoto. *Phys. Rev. Lett.* **81**, 3611 (1998).
- [24] M. D. Lukin, P. R. Hemmer, M. L offler, & M. O. Scully. *Phys. Rev. Lett.* **81**, 2675(1988).
- [25] V. Boyer, C. F. McCormick, E. Arimondo, and P. D. Lett. *Phys. Rev. Lett.* **99**, 143601(2007).
- [26] N. B. Philips, A. V. Gorshkov, and I. Novikova. *J. Mod. Opt.* **56**, 1916-1925(2009).
- [27] N. Lauk, C. O'Brien, and M. Fleischhauer. *Phys. Rev. A*, **88**, 013823(2013).
- [28] M. T. Turnbull, P. G. Petrov, C. S. Embrey, A. M. M. Taylor and V. Boyer *Phys. Rev. A*, **88**, 033845(2013).
- [29] Supplementary materials of this paper.
- [30] B.-W. Shiau, M.-C. Wu, C.-C. Lin, and Y.-C. Chen. *Phys. Rev. Lett.* **106**, 193006(2011).
- [31] J. M. Amini and H. Gould. *Phys. Rev. Lett.* **91**, 153001(2003).
- [32] Y.-F. Hsiao, H.-S. Chen, P.-J. Tsai, and Y.-C. Chen. *Phys. Rev. A*, **90**, 055401(2014).
- [33] Bo Zhao, Y.-A. Chen, X.-H. Bao, T. Strassel, C.-S. Chuu, X.-M. Jin, J. Schmiedmayer, Z.-S. Yuan, S. Chen and J.-W. Pan. *Nat. Phys.* **5**, 95(2008).
- [34] S.-W. Su, Y.-H. Chen, S.-C. Gou, and I. A. Yu, *J. Phys. B* **44**, 165504(2011).
- [35] M. Mitsunaga, M. Yamashita, and H. Inoue. *Phys. Rev. A* **62**, 013817(2000).
- [36] Y.-F. Chen, Y.-C. Liu, Z.-H. Hsai, S.-H. Wang, and I. A. Yu. *Phys. Rev. A*, **72**, 033812(2005).
- [37] Y.-F. Chen, Y.-M. Kao, W.-H. Lin, and I. A. Yu. *Phys. Rev. A* **74**, 063807(2006).
- [38] Y. H. Chen, M. J. Lee, I. C. Wang, and I. A. Yu. *Phys. Rev. A* **88**, 023805(2013).
- [39] T. Peters, Y.-H. Chen, J.-S. Wang, Y.-W. Lin, and I. A. Yu. *Opt. Express* **17**, 6665(2009).
- [40] Y.-F. Hsiao, P.-J. Tsai, C.-C. Lin, Y.-F. Chen, I.A. Yu, and Y.-C. Chen. *Opt. Lett.* **39**, 3394(2014).
- [41] C.-S. Chuu, T. Strassel, B. Zhao, M. Koch, Y.-A. Chen, S. Chen, Z.-S. Yuan, J. Schmiedmayer, and J.-W. Pan. *Phys. Rev. Lett.* **101**, 120501(2008).

# EIT-based photonic memory with near-unity storage efficiency: Supplementary Materials

## Experimental setup and sequence

Our experiment is based on a vapor-cell two-dimensional magneto-optical trap (MOT) of cesium. The total power of the trapping and repumping beams after the single mode fiber are  $\sim 350$  and  $50$  mW, respectively. The diameters for both beams are  $\sim 22$  mm. We typically trap  $\sim 5 \times 10^9$  atoms with a cigar-shaped cloud of dimensions  $\sim 3 \times 3 \times 14$  mm. To increase the optical depth, we have utilized temporally dark and magnetically compressed MOT techniques, and Zeeman-state optical pumping to prepare population in the single Zeeman state  $|F = 3, m = 3\rangle$ .

Two master lasers are locked to cesium saturation absorption spectrometer at  $D_1$  and  $D_2$  line, respectively. The  $D_1$  and  $D_2$  control laser are injection locked by the corresponding master laser. Part of each master light passes through a fiber electro-optic modulator (EOM) operated around 9 GHz and its +1 sideband injection-lock the  $D_1$  and  $D_2$  probe laser, respectively. Some acousto-optic modulators (AOMs) are used for power switching and frequency shifting such that the frequencies of the control beams are on the  $|F = 4\rangle \rightarrow |F' = 4\rangle$  transition and that of the probe beams are on the  $|F = 3\rangle \rightarrow |F' = 4\rangle$  transition of the  $D_1$  and  $D_2$  line, respectively. With the injection locking technique and good frequency stabilities for the AOM and EOM drivers, the mutual coherence of the control and probe lasers is kept to a good level, which is one of the key to obtain a small ground-state decoherence rate.

The linewidth of the master laser also plays an important role in obtaining a high SE. During the early operations of the experiment, we used a 895 nm homemade external cavity diode laser (ECDL) as the  $D_1$  line master laser. The laser linewidth was observed to drift within the range of 200 kHz to 3 MHz, measured by the delayed self-heterodyne method[S2]. The long-term laser frequency fluctuation may also contribute to the overall laser linewidth since the data averaging takes about 34 s. From the fluctuation of the error signal of the saturation absorption spectrometer for laser frequency stabilization, we estimate that the laser central frequency fluctuation is  $\sim 1$  MHz. At an OD of  $\sim 300$ , the SE can vary up to 6% within that linewidth range. The variation in SE is consistent with Eq. (1) if one includes the laser linewidth ( $\Gamma_L$ ) into the decoherence rate  $\gamma_{31} = \frac{\Gamma + \Gamma_L}{2}$ . During the later operations, we have replaced the 895 nm master laser by a commercial one (Toptica DL pro), whose linewidth is checked to be less 100 kHz during the whole operation. Our 852-nm master laser is a home-made ECDL. Its linewidth is measured to be less than 1 MHz. In the data of Fig 3 (a) and (b), we attribute  $\Gamma_L$  of  $0.2\Gamma$  and  $0.4\Gamma$  for the  $D_1$  and  $D_2$  system, respectively. The theoretical curves for  $D_1$  and  $D_2$  system with  $\gamma_{31}$  of  $0.6\Gamma$  and  $0.7\Gamma$  agree with the data reasonably well.

The experiment runs at a periodic manner with the slow and stored light measurements taken at 1.5 ms after the quadrupole magnetic field of the MOT is turned off to reduce the ground-state decoherence rate due to the inhomogeneity of the magnetic field. Some electronics are used to reduce the  $e^{-1}$  turn-off time to 200  $\mu$ s. We avoid to put metallic components near the cell region to minimize the induced eddy currents. Three pairs of magnetic compensation coils are used to null the stray magnetic field. Optimization of the stray magnetic field compensation is performed by iteratively fine tuning of the currents through the compensation coils and prolonging the storage time. To reduce the ac magnetic noise due to the 60 Hz power line, the measurement is synchronized to it and is run at a 7.5 Hz repetition rate.

When taking the EIT spectrum, a probe pulse of square waveform of 100  $\mu$ s duration are applied. The probe power at 35-40  $\mu$ s after being turned on are measured to determine the probe transmission in order to obtain the steady-state response. By varying the probe frequency through an double-passed AOM and repeating the measurement, the EIT spectrum is obtained.

## Determination of the experimental parameters

. The parameters  $D$ ,  $\Omega_c$  and  $\gamma$  are determined by fitting the slow light traces to the calculations based on solving the Maxwell-Bloch equations for a given  $\gamma_{31}$ [S1]. At a relatively large OD when the broadening factor  $\beta$  is close to 1, the uncertainties of fitting parameters become significant due to the sharp dependence of the fitting parameters  $\Omega_c$  and  $D$  to a slight variation in  $\beta$ . Because the fluctuation in OD and control intensity affects the group delay and we average the slow light trace for 256 times, these result in a slightly larger in  $\beta$  compared to the single shot data. The fitting parameters are not reliable at large ODs. At a relatively small OD,  $\beta$  is much larger than 1. For example,  $\beta \sim 1.8$  for an OD of 50 with  $\zeta=2.7$ . The effect of fluctuation in group delay and data averaging on  $\beta$  and thus the fitting parameters  $D$  and  $\Omega_c$  is relatively small at a smaller OD. Therefore, we first fit the slow light trace at a smaller

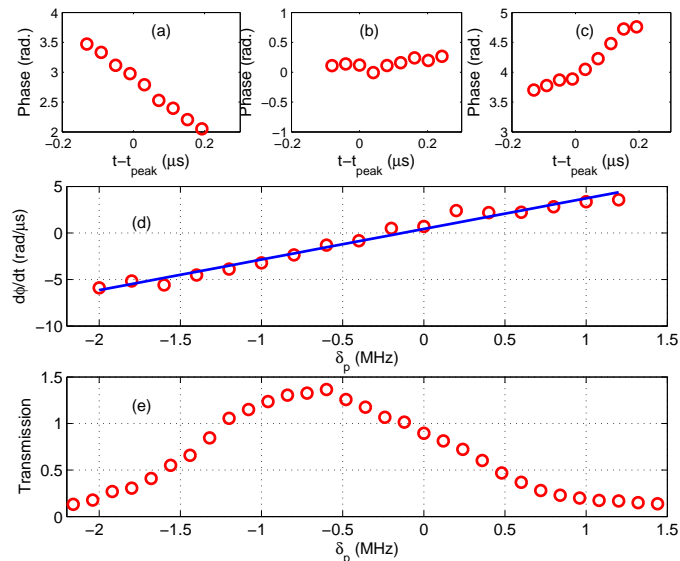


FIG. S1: Dispersive effect of atomic clouds on the collection optics. (a)(b)(c) Phase shifts for different parts of the probe pulses for  $\delta_p$  equal to -1.4, -0.2 and 1.2 MHz, respectively. (d) The phase derivative over time,  $d\phi/dt$ , versus  $\delta_p$ . The blue line is a linear fit to the data. Its intersection to the horizontal axis indicates the true zero two-photon detuning. (e) The corresponding steady-state probe transmission after the etalon filter under a situation in which the collection optics are not well optimized. At the zero two-photon detuning, the probe transmission is near unity. The larger than unity transmission is due to the dispersive effect of the atomic cloud and the variation in collection efficiency of filtering optics, as explained in the main contexts.

OD to obtain a full set of parameters  $D$ ,  $\Omega_c$ , and  $\gamma$ . We have monitored the power of the control field during the experiment. For the slow light traces with higher ODs,  $\Omega_c$  is obtained by the power scaling law and is not treated as a fitting parameter while the other two parameters  $D$  and  $\gamma$  are obtained by the slow light fitting.

### Filtering optics of the control beam

. We have kept the angle  $\theta = 0.5^\circ$  between the control and probe beams to reduce the decoherence effect of the atomic motions. With such a small angle, the leakage of the strong control beam into the PMT for probe detection become an issue. Many arrangements are used to minimize this leakage. First, the control beam is kept well collimated and the probe beam is focused around the atomic cloud region. The  $e^{-2}$  diameter for the control beam is 1.1 mm and the  $e^{-2}$  waist of the probe beam is  $50 \mu\text{m}$ . After passing through the cell, there is a lens to make the probe beam collimated but to focus the control beam. Around the focal point of the control beam, a window with a small black dot of diameter  $300 \mu\text{m}$  is used to reduce the control beam leakage by  $\sim 38$  dB. The probe beam propagates around 4 m and pass through two iris before it arrives at a temperature-stabilized etalon filter(Quantaser FPE001). The etalon reduces the control leakage by 35 dB and its maximum transmission is 58%. The probe output after the etalon is coupled into a multimode fiber and detected by a PMT (Hamamatsu R636-10). The probe transmission efficiency of the cell window, window with a black dot, and fiber coupling are 95%, 82%, and 80%, respectively. The probe beam propagates in ambient environment for  $\sim 4$  m and we have observed  $\sim 13\%$  loss due to the water absorption loss around 894.6 nm[S3]. The overall collection efficiency of the probe beam after these filtering components is 31%.

However, one should be cautious that this collection efficiency might vary under the presence of cold atoms and might lead to problematic determination of the SE. The transverse profile of the probe beam may vary after passing through the atomic media if there is a finite two-photon detuning and if there is an inhomogeneity in the transverse profile of the control intensity and/or atomic density. If the mode matching condition of the etalon filter is not well optimized, the transmission efficiency of the filtering optics may vary significantly versus the two-photon detuning which may lead to asymmetry and even gain in the apparent EIT spectrum. This may leads to problematic determination of the EIT resonant frequency and thus the SE if one determines the EIT resonant frequency just by the transmission peak. While the dispersive effect is null at the exact EIT resonance, a more precisely way to determine the actual EIT resonant frequency is based on the phase measurement using the beatnote interferometer[S4]. As shown in Fig. 1 (c), a reference beam which is red-detuned from the probe frequency by 200 MHz is combined with the probe

pulse and then shoot the atomic clouds. We redirect the probe and reference light into an avalanche photodetector (1GHz bandwidth, Hamamatsu C5658) before passing through the etalon filter. The beatnote traces are recorded and analyzed. The EIT resonance can be precisely determined if the slope of the phase versus time for different portions of the probe pulse is flat[S5]. One can then precisely determine the EIT resonance and obtain a reliable measurement of the SE.

As an example, Fig. S1(e) depicts the probe transmission among the EIT transparent peak when the mode matching condition of the etalon is not well optimized. An apparent gain as large as 40% is observed. However, the transmission peak is not the actual EIT resonance as can be seen by the phase measurement. Fig. S1(a) (b) and (c) depict the phase versus time among the probe pulses for three detunings at -1.4, -0.2 and 1.2 MHz, respectively. Fig. S1 (d) shows the phase slope versus probe detuning. The blue line is a linear fit of the data. The zero crossing for probe detuning at -0.1 MHz determines the actual EIT resonance. At such a detuning, there is almost no apparent probe gain as can be seen in Fig. S1(e). For the case with the mode matching of the etalon filter being well optimized, there is no such a large apparent gain in the EIT spectrum with Fig. 3(a) as an example. We have used the phase measurement to make sure the probe is at the actual EIT resonance for all the SE data we took.

### Slow light transmission in a three-level $\Lambda$ -type system

In a  $\Lambda$ -type three-level system, the classical probe field (with frequency  $\omega_p$  and Rabi frequency  $\Omega_p$ ) drives the ground state  $|1\rangle$  to the excited state  $|3\rangle$ , and the classical control field (with frequency  $\omega_c$  and Rabi frequency  $\Omega_c$ ) drives another ground state  $|2\rangle$  to  $|3\rangle$ , where the Rabi frequencies  $\Omega_{p(c)} = \vec{d}_{13(23)} \cdot \vec{E}_{p(c)}/\hbar$  are assumed to be real. The transition frequencies from state  $|1\rangle$  and  $|2\rangle$  to  $|3\rangle$  are denoted as  $\omega_{31}$  and  $\omega_{32}$ , respectively. Under the rotating-wave approximation and in the interaction picture, the Hamiltonian can be expressed as

$$\begin{bmatrix} 0 & 0 & -\frac{\hbar\Omega_p}{2} \\ 0 & -\hbar\delta_2 & -\frac{\hbar\Omega_c}{2} \\ -\frac{\hbar\Omega_p}{2} & -\frac{\hbar\Omega_c}{2} & -\hbar\delta_p \end{bmatrix}, \quad (\text{S1})$$

where  $\delta_{p(c)} = \omega_{p(c)} - \omega_{31(32)}$  is the probe (control) detuning and  $\delta_2 = \delta_p - \delta_c$  is the two-photon detuning. The relaxation terms for the density matrix are denoted as,

$$\begin{bmatrix} \Gamma_{31}\sigma_{33} & -\gamma_{12}\sigma_{12} & -\gamma_{13}\sigma_{13} \\ -\gamma_{21}\sigma_{21} & \Gamma_{32}\sigma_{33} & -\gamma_{23}\sigma_{23} \\ -\gamma_{31}\sigma_{31} & -\gamma_{32}\sigma_{32} & -\Gamma\sigma_{33} \end{bmatrix}, \quad (\text{S2})$$

with  $\Gamma = \Gamma_{31} + \Gamma_{32}$ . Under the weak probe assumption ( $\Omega_p \ll \Omega_c$ ), the relevant first-order optical Bloch equations (OBEs) are,

$$\frac{d\sigma_{31}}{dt} = (i\delta_p - \gamma_{31})\sigma_{31} + \frac{i}{2}\Omega_c\sigma_{21} + \frac{i}{2}\Omega_p, \quad (\text{S3})$$

$$\frac{d\sigma_{21}}{dt} = (i\delta_2 - \gamma_{21})\sigma_{21} + \frac{i}{2}\Omega_c\sigma_{31}. \quad (\text{S4})$$

Under the slowly-varying envelope approximation, the Maxwell equation for the probe field is,

$$\frac{\partial\Omega_p}{\partial z} + \frac{1}{c}\frac{\partial\Omega_p}{\partial t} = i\frac{D\Gamma}{2L}\sigma_{31}, \quad (\text{S5})$$

where  $D$  is the optical depth of the atomic media and  $L$  is the media length. Since  $\Omega_p \ll \Omega_c$ , one can treat  $\Omega_c$  as a constant. Taking the Fourier transform on the two atomic coherences ( $\sigma_{31}$  and  $\sigma_{21}$ ) and the probe Rabi frequency  $\Omega_p$  to frequency domain, e.g.  $R_{31} = 1/\sqrt{2\pi}\int_{-\infty}^{\infty}\sigma_{31}e^{i\omega t}dt$ , the OBEs and Maxwell equation read as follows:

$$-i\omega R_{31} = (i\delta_p - \gamma_{31})R_{31} + \frac{i}{2}\Omega_c R_{21} + \frac{i}{2}W_p, \quad (\text{S6})$$

$$-i\omega R_{21} = (i\delta_2 - \gamma_{21})R_{21} + \frac{i}{2}\Omega_c R_{31}, \quad (\text{S7})$$

$$\frac{\partial W_p}{\partial z} - \frac{i\omega}{c} W_p = i \frac{D\Gamma}{2L} R_{31}. \quad (\text{S8})$$

By solving Eqs.(S6) and (S7), one obtains the expression for  $R_{31}$ ,

$$R_{31}(\omega, z) = \frac{-[i(\omega + \delta_2) - \gamma_{21}]iW_p(\omega, z)/2}{[i(\omega + \delta_p) - \gamma_{31}][i(\omega + \delta_2) - \gamma_{21}] + \Omega_c^2/4}. \quad (\text{S9})$$

Putting this into Eq.(S8) and integrating over  $z$ , one obtains the solution of  $W_p(\omega, z)$ ,

$$W_p(\omega, z) = W_p(\omega, 0) \exp\left[\frac{i\omega z}{c} + \frac{Dz\Gamma}{4L} \frac{i(\omega + \delta_2) - \gamma_{21}}{[i(\omega + \delta_p) - \gamma_{31}][i(\omega + \delta_2) - \gamma_{21}] + \Omega_c^2/4}\right]. \quad (\text{S10})$$

The steady-state EIT transmission spectrum can be obtained by setting  $\omega = 0$  and  $z = L$  in Eq.(S10), which is

$$T(\delta_p) = \text{Exp}\left\{\frac{D\Gamma}{2} \text{Re}\left(\frac{i(\delta_p - \delta_c) - \gamma_{21}}{(i\delta_p - \gamma_{31})(i\delta_p - \delta_c) - \gamma_{21}} + \frac{\Omega_c^2}{4}\right)\right\}, \quad (\text{S11})$$

where  $\text{Re}()$  stands for the real part of the expression inside the bracket. From Eq.(S11) with  $\delta_c = 0$ , one can show that the FWHM frequency width of the EIT transmission spectrum is,

$$\Delta\omega_{EIT} \cong \sqrt{\frac{\ln 2}{2}} \frac{\Omega_c^2}{\sqrt{D\gamma_{31}\Gamma}}, \quad (\text{S12})$$

where we assume  $\Omega_c \gg \Delta\omega_{EIT}$  and  $\Omega_c \gg 4\gamma_{31}\gamma_{21}$ . We assume the input probe pulse is a Gaussian waveform with an intensity FWHM duration of  $T_p$ , i.e.

$$\Omega_p(t, z = 0) = \Omega_{p0} \exp(-2\ln 2 \frac{t^2}{T_p^2}). \quad (\text{S13})$$

The Fourier transform of the input probe pulse can be calculated to be,

$$W_p(\omega, z = 0) = \frac{\Omega_{p0} T_p}{\sqrt{4\ln 2}} \exp(-\frac{\omega^2 T_p^2}{8\ln 2}). \quad (\text{S14})$$

Putting Eq.(S14) into Eq.(S10) and taking the inverse Fourier transform, one obtains the solution of the probe pulse after passing through an EIT media as,

$$\Omega_p(t, z = L) = \frac{1}{\sqrt{2\pi}} \frac{\Omega_{p0} T_p}{\sqrt{4\ln 2}} \int_{-\infty}^{\infty} d\omega \exp\left\{-i\omega t - \frac{\omega^2 T_p^2}{8\ln 2} + \frac{i\omega L}{c} + \frac{(i(\omega + \delta_2) - \gamma_{21})D\Gamma}{4(i(\omega + \delta_p) - \gamma_{31})(i(\omega + \delta_2) - \gamma_{21}) + \Omega_c^2}\right\}. \quad (\text{S15})$$

The output probe pulse with arbitrary parameters can be numerically calculated by this relation. Under the special case with  $\delta_p = 0 = \delta_c$ , one can expand the EIT media response function  $f(\omega) = i \frac{D\Gamma}{2} \frac{R_{31}}{W_p}$  with respect to  $\omega$  as follows,

$$f(\omega) = \frac{(i\omega - \gamma_{21})D\Gamma}{4(i\omega - \gamma_{31})(i\omega - \gamma_{21}) + \Omega_c^2}, \quad (\text{S16})$$

$$= \frac{-\gamma_{21}D\Gamma}{\Omega_c^2 + 4\gamma_{21}\gamma_{31}} + i \frac{D\Gamma(\Omega_c^2 - 4\gamma_{21}^2)}{(\Omega_c^2 + 4\gamma_{21}\gamma_{31})^2} \omega - \frac{4D\Gamma(\gamma_{31}\Omega_c^2 + 2\gamma_{31}^2\gamma_{21} - 4\gamma_{21}^3)}{(\Omega_c^2 + 4\gamma_{21}\gamma_{31})^3} \omega^2 + O(\omega^3) \quad (\text{S17})$$

$$\cong -\frac{\gamma_{21}D\Gamma}{\Omega_c^2} + i \frac{D\Gamma}{\Omega_c^2} \omega - \frac{4D\gamma_{31}\Gamma}{\Omega_c^4} \omega^2 + O(\omega^3), \quad (\text{S18})$$

where it is assumed that  $\Omega_c^2 \gg 4\gamma_{21}\gamma_{31}$ . If we keep the dispersion relation up to the  $\omega^2$  term, Eq.(S15) can be analytically integrated to become,

$$\Omega_p(t, z = L) = \frac{\Omega_{p0}}{\beta} \exp(-\gamma \frac{D\Gamma}{\Omega_c^2}) \exp[-2\ln 2 (\frac{t - T_d}{\beta T_p})^2], \quad (\text{S19})$$

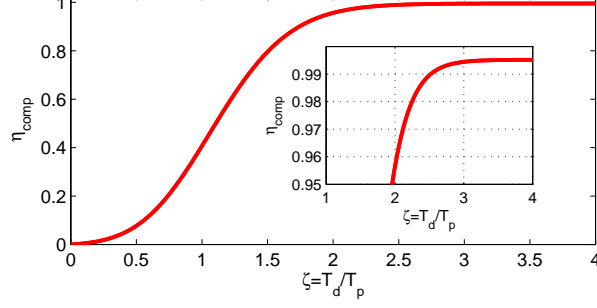


FIG. S2:  $\eta_{comp}$  versus  $\zeta$  for the case with  $\kappa = 1.1$  and  $D=100$ .

where we have defined

$$\beta = \sqrt{1 + \frac{32 \ln 2 D \Gamma \gamma_{31}}{T_p^2 \Omega_c^2}} \quad (\text{S20})$$

$$T_d = \frac{L}{v_g} = \frac{L}{c} + \frac{D\Gamma}{\Omega_c^2}. \quad (\text{S21})$$

From Eq.(S19), it is evident to see that the amplitude of the slow light pulse decreases by a factor of  $\beta$  times a factor due to the finite ground-state decoherence rate and its duration broadens by a factor of  $\beta$ . If the group velocity  $v_g \ll c$ , then the group delay  $T_d \cong \frac{D\Gamma}{\Omega_c^2}$ . Integrating Eq.(S19) over the time, one can obtain the slow light energy transmission as follows:

$$T = \frac{\exp(-2\gamma_{21}T_d)}{\beta} = \frac{\exp(-2\gamma_{21}T_d)}{\sqrt{1 + 32 \ln 2 \frac{\gamma_{31}}{\Gamma} \frac{\zeta^2}{D}}}, \quad (\text{S22})$$

where  $\zeta = T_d/T_p$ . Combining this relation with Eq.(S12), one obtains,

$$T = \frac{\exp(-2\gamma_{21}T_d)}{\sqrt{1 + \left(\frac{4 \ln 2}{T_p \Delta \omega_{EIT}}\right)^2}}. \quad (\text{S23})$$

It is evident to see that the finite ground-state decoherence rate and the finite EIT transparent bandwidth are the two limiting factors for the slow light transmission.

### Efficiency due to cutoff of the pluse edges during storage

At time  $t = 0$ , the peak of a Gaussian probe pulse enters the media. At time  $t = t_c$ , one turns off the control field and stores the major part of the pulse inside the media. A small portion of the front edge of the pulse has passed through the media, while a small portion of the rear edge has not yet arrived at the media. These two parts of pulse cannot be stored into the media. The fractional energy being stored can be written as follows:

$$\eta_{comp} = 1 - \frac{\int_{-\infty}^{t_c} \Omega_p^2(z=0, t) dt}{\int_{-\infty}^{\infty} \Omega_p^2(z=0, t) dt} - \frac{\int_{t_c}^{\infty} \Omega_p^2(z=L, t) dt}{\int_{-\infty}^{\infty} \Omega_p^2(z=L, t) dt}. \quad (\text{S24})$$

Using Eqs. (S13) and (S19) and the definition of the error function, one obtains

$$\eta_{comp} = \frac{1}{2} [\text{erf}(2\sqrt{\ln 2} \kappa) + \text{erf}(2\sqrt{\ln 2} \frac{\zeta - \kappa}{\beta})], \quad (\text{S25})$$

where  $\kappa = \frac{t_c}{T_p}$ ,  $\zeta = \frac{T_d}{T_p}$ . With a large enough OD, it is possible to find that with  $\kappa$  and  $\zeta$  larger than a critical value then  $\eta_{comp}$  can be larger than 0.99. With a larger OD, the critical value for  $\zeta$  at a given  $\kappa$  can be smaller. Fig. S2 shows an example for  $\eta_{comp}$  versus  $\zeta$  for  $\kappa=1.1$  and OD=100.

### Slow light transmission in a N-type four-level system

Considering the off-resonantly excitation of the control field from the state  $|2\rangle$  to an additional excited state  $|4\rangle$  as that shown in Fig.1 (a), the level scheme is a  $N$ -type four-level system in which the control field also acting the role of the switching field which drives  $|2\rangle \rightarrow |4\rangle$  transition. In the  $N$ -type system, the probe field has one additional loss channel due to the multi-photon process from state  $|1\rangle \rightarrow |3\rangle \rightarrow |2\rangle \rightarrow |4\rangle$  and then spontaneous decay. The Rabi frequency of the switching field is  $\Omega_s = \epsilon\Omega_c$ , where  $\epsilon$  is the ratio of the Clebsch-Gordon coefficient of the switching transition to that of the control transition. In the level scheme of Fig.1(a),  $\epsilon = \sqrt{48/7}$ .

Similar to the procedures before, one can write down the frequency-domain first-order perturbative OBEs as,

$$-i\omega R_{31} = (i\delta_p - \gamma_{31})R_{31} + \frac{i\Omega_c}{2}R_{21} + \frac{i}{2}W_p, \quad (\text{S26})$$

$$-i\omega R_{21} = (i\delta_2 - \gamma_{21})R_{21} + \frac{i\Omega_c}{2}R_{31} + \frac{i\Omega_s}{2}R_{41}, \quad (\text{S27})$$

$$-i\omega R_{41} = (i\delta_3 - \gamma_{41})R_{41} + \frac{i\Omega_s}{2}R_{21}, \quad (\text{S28})$$

where the three-photon detuning  $\delta_3 = \delta_p - \delta_c + \delta_s$  and  $\delta_s = \omega_s - \omega_{42}$ . By solving Eqs.(S26)-(S28), one obtains,

$$R_{31} = -\frac{iW_p}{2} \frac{[i(\omega + \delta_2) - \gamma_{21}][i(\omega + \delta_3) - \gamma_{41}] + \Omega_s^2/4}{[i(\omega + \delta_p) - \gamma_{31}]\{[i(\omega + \delta_2) - \gamma_{21}][i(\omega + \delta_3) - \gamma_{41}] + \Omega_s^2/4\} + [i(\omega + \delta_3) - \gamma_{41}]\Omega_c^2/4} \quad (\text{S29})$$

Putting it into Eq. (S8) and setting  $\omega = 0$ , one obtains the steady-state spectrum for the N-type four-level system as,

$$T(\delta_p) = \text{Exp}\left\{\frac{D\Gamma}{2} \text{Re}\left(\frac{(i\delta_2 - \gamma_{21})(i\delta_3 - \gamma_{41}) + \Omega_s^2/4}{(i\delta_p - \gamma_{31})[i(\delta_2 - \gamma_{21})(i\delta_3 - \gamma_{41}) + \Omega_s^2/4] + (i\delta_3 - \gamma_{41})\Omega_c^2/4}\right)\right\} \quad (\text{S30})$$

By dividing both the numerator and denominator in Eq.(S29) by  $i(\omega + \delta_3) - \gamma_{41}$  and comparing the result with Eq.(S9) of the three-level system, one finds that it has the same form as  $R_{31}$  in the  $\Lambda$ -type system except that in the denominator and numerator the term  $i\delta_2 - \gamma_{21}$  is modified to

$$i\delta_2 - \gamma_{21} + \frac{\Omega_s^2}{4(i\delta_3 - \gamma_{41})} = i\left[\delta_2 - \frac{\Omega_s^2\delta_3}{4(\delta_3^2 + \gamma_{41}^2)}\right] - \left[\gamma_{21} + \frac{\Omega_s^2\gamma_{41}}{4(\delta_3^2 + \gamma_{41}^2)}\right]. \quad (\text{S31})$$

In the case with  $\delta_c = 0$  and in the limit  $\delta_s \gg \delta_p$  and  $\delta_s \gg \gamma_{41}$ ,  $R_{31}$  of the N-type system is similar to that of  $\Lambda$ -type system with the effective two-photon detuning and effective ground-state decoherence rate replaced by the relations,

$$\delta_{2,eff} \cong \delta_2 - \frac{\Omega_s^2}{4\delta_s}, \quad (\text{S32})$$

$$\gamma_{21,eff} \cong \gamma_{21} + \frac{\Omega_s^2\gamma_{41}}{4\delta_s^2}. \quad (\text{S33})$$

The physical meaning of these two relations are clear. Due to the off-resonant coupling of the control field on the transition  $|2\rangle \rightarrow |4\rangle$ , it introduces an ac Stark shift ( $\sim -\frac{\Omega_s^2}{4\delta_3}$ ) on state  $|2\rangle$  and an additional decoherence rate ( $\frac{\Omega_s^2\gamma_{41}}{4\delta_s^2}$ ) on  $\gamma_{21}$  due to the optical excitation and the spontaneous decay. However, one should be aware that the previous approximation of  $R_{31}$  is only valid with  $\delta_p \ll \delta_s$ . To be more precisely, we fit the EIT spectra of  $D_2$  line to the complete lineshape, i.e. Eq.(S30), to determine the parameters  $\gamma_{21}$ ,  $D$  and  $\Omega_c$ . Putting Eqs. (S29) and S14 into Eq.(S8), one can numerically calculate the output pulse after passing through a  $N$ -type media with arbitrary parameters.

Fig. S3 shows some representative EIT spectra for both  $D_1$  and  $D_2$  schemes. Two trends are clearly seen. First, the degree of transparency in the EIT transparent peaks for the  $D_1$  scheme is much higher than that in the  $D_2$

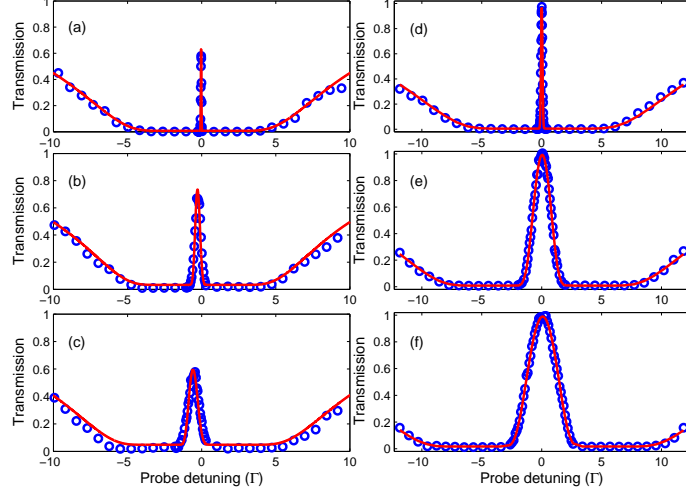


FIG. S3: Some representative EIT spectra for the  $D_2$  ((a) to (c)) and  $D_1$  ((d) to (f)) schemes. The red lines in (a)(b), and (c) are the fitting curves to Eq. (S30) with  $\gamma_{31}=\gamma_{41}=0.7\Gamma$ . The fitting parameters  $\{D, \gamma_{21}, \Omega_c\}$  for (a) (b), and (c) are  $\{232(14), 0.0005(2)\Gamma, 1.01(2)\Gamma\}$ ,  $\{204(18), 0.0022(4)\Gamma, 2.81(6)\Gamma\}$ , and  $\{257(28), 0.0098(32)\Gamma, 4.10(8)\Gamma\}$ , respectively. The red lines in (d) to (f) are the fitting curves to Eq. (S11) with  $\gamma_{31}=0.6\Gamma$ . The fitting parameters  $\{D, \gamma_{21}, \delta_c, \Omega_c\}$  are  $\{478(13), 0.00015(5)\Gamma, 0.0075(8)\Gamma, 2.05(3)\Gamma\}$ ,  $\{544(18), 0.00030(39)\Gamma, 0.043(6)\Gamma, 7.31(6)\Gamma\}$ , and  $\{653(34), 0.00076(64)\Gamma, 0.086(11)\Gamma, 10.01(11)\Gamma\}$  respectively. The quantities in the brackets are the  $2\sigma$  standard deviation of the fitting parameters.

scheme. Second, the EIT transparent peaks for the  $D_2$  scheme have clear shifts when the control intensity is stronger. The shifts for the  $D_1$  spectra is very small even for the strongest control intensity. The reason for these two trends is the same. In the  $D_2$  scheme, the off-resonant excitations of the control field in the  $|2\rangle \rightarrow |4\rangle$  transition is much stronger with relatively small detuning  $\delta_s$  of 251.0916 MHz. From the fitting of the  $D_1$  EIT spectra to Eq. (S11), the parameters  $\{D, \Omega_c, \gamma_{21}, \delta_c\}$  can be determined. The EIT resonance shift is represented by the fitting parameter  $\delta_c$ . For the  $D_2$  spectra, we still fit to Eq. (S11) first just to get the parameter  $\delta_c$  for resonance shifts. We then fit the same spectra to Eq. (S30) to determine the parameters  $\{D, \Omega_c, \gamma_{21}\}$  by setting  $\delta_c=0$ . The systematic variations of  $\gamma_{21}$  and resonance shift versus the control power are shown in Fig. 2 of the main contexts. The theoretical line of  $\gamma_{21}$  and resonance shifts for the  $D_2$  line shown in Fig. 2 are calculated by Eqs. (S33) and (S32).

### Semi-classical calculation of the four-wave mixing

For the energy level illustrated in Fig. 1(b) of the main context, the off-resonant excitation of the control field on the probe transition can act as a pumping field and induces a four-wave mixing process through absorbing the pump photons, emitting the Stoke photons, absorbing the control photons and emitting the probe photons. FWM induces a probe gain and introduces quantum noise which reduces the fidelity of a quantum memory based on an EIT medium. A better way to evaluate the effect of the FWM on the EIT-based memory would be through calculation of the fidelity based on the Bloch-Langevin and Maxwell equations[S6]. However, this calculation is very involved. Since the reduction in the fidelity is monotonically proportional to the probe gain[S6], we use the semiclassical Bloch-Maxwell equations to calculate the FWM probe gain to evaluate the effect of the FWM in our system. We perform the calculation both in the steady-state and pulse regime. For the pulse calculation, the complete optical Bloch equations and the Maxwell equation are numerically calculated under the assumption of perfect phase matching. The calculated FWM gain can be considered as an upper bound of the experimental results. Fig. 5(a) in the main context is based on this calculation. For the steady-state calculation, the analytic expressions are obtained under the weak probe and idler perturbation. The phase mismatching is also considered for evaluation of the dependence of the FWM gain on the probe detuning and its intersection angle with the control beam[S7]. The calculation is similar to that in [S7], but we relieve the assumption that the Rabi frequencies for the control field on the two transitions it drives are the same. Figs. 5(b),(c) and (d) in the main context are calculated using the steady state formula described in this section.

Although our energy level scheme involves three levels only, a four-level model is used to facilitate our calculation. In the limit of far pump detuning (which is valid in our case with a detuning of  $\sim 9.2$  GHz, the basic equations for the

three and four level model are the same, except for a difference in the ac-Stark shift which plays a minor role[S6]. The energy levels and notations follow that in [S7]. However, it should be noted that the definition of the probe detuning  $\delta_p$  in ?? and this section differ by a negative sign to those elsewhere of the main context and other sections in this supplementary material. The calculation shown in Fig. 5 of the main context uses the formulation in this section but the notation  $\delta_p$  there follows the previous convention. Including the time dependence, the Hamiltonian of the system is

$$\begin{bmatrix} 0 & 0 & -\frac{\hbar\Omega_p^*}{2}e^{i\omega_p t} & -\frac{\hbar\Omega_d^*}{2}e^{i\omega_c t} \\ 0 & \hbar\omega_{21} & -\frac{\hbar\Omega_c^*}{2}e^{i\omega_c t} & -\frac{\hbar\Omega_i^*}{2}e^{i\omega_i t} \\ -\frac{\hbar\Omega_p}{2}e^{-i\omega_p t} & -\frac{\hbar\Omega_c}{2}e^{-i\omega_c t} & \hbar\omega_{31} & 0 \\ -\frac{\hbar\Omega_d}{2}e^{-i\omega_c t} & -\frac{\hbar\Omega_i}{2}e^{-i\omega_i t} & 0 & \hbar\omega_{41} \end{bmatrix}. \quad (\text{S34})$$

To incorporate the phase matching issue, the position dependent phase factor should be included in the Rabi frequencies, e.g.  $\Omega_p$  should be replaced by  $\Omega_p e^{i\vec{k}_p \cdot \vec{r}}$  and so on. However, for clarity of notation, we will do that after the solution of the density matrix elements is reached. Considering the unitary transformation

$$T = \begin{bmatrix} 1 & 0 & 0 & 0 \\ 0 & e^{i(\omega_p - \omega_c)t} & 0 & 0 \\ 0 & 0 & e^{i\omega_p t} & 0 \\ 0 & 0 & 0 & e^{i\omega_c t} \end{bmatrix}, \quad (\text{S35})$$

the Hamiltonian in the new basis is  $H' = THT^\dagger + i\hbar\frac{dT}{dt}T^\dagger$ . To completely eliminate the explicit time independence in the Hamiltonian, the frequencies of the control, probe and idler need to satisfy

$$2\omega_c = \omega_p + \omega_i, \quad (\text{S36})$$

which is the energy conservation condition of the FWM process. The Hamiltonian in the new basis then becomes

$$H = \hbar \begin{bmatrix} 0 & 0 & -\frac{\Omega_p^*}{2} & -\frac{\Omega_d^*}{2} \\ 0 & -\delta_2 & -\frac{\Omega_c^*}{2} & -\frac{\Omega_i^*}{2} \\ -\frac{\Omega_p}{2} & -\frac{\Omega_c}{2} & -\delta_p & 0 \\ -\frac{\Omega_d}{2} & -\frac{\Omega_i}{2} & 0 & -\delta_d \end{bmatrix}. \quad (\text{S37})$$

The evolution equations for the density matrix elements are,

$$\dot{\sigma}_{11} = \frac{i}{2}(\Omega_p^* \sigma_{31} + \Omega_d^* \sigma_{41} - \Omega_p \sigma_{13} - \Omega_d \sigma_{14}) + \Gamma_{31} \sigma_{33} + \Gamma_{41} \sigma_{44}, \quad (\text{S38})$$

$$\dot{\sigma}_{22} = \frac{i}{2}(\Omega_c^* \sigma_{32} + \Omega_i^* \sigma_{42} - \Omega_c \sigma_{23} - \Omega_i \sigma_{24}) + \Gamma_{32} \sigma_{33} + \Gamma_{42} \sigma_{44}, \quad (\text{S39})$$

$$\dot{\sigma}_{33} = \frac{i}{2}(\Omega_p \sigma_{13} + \Omega_c \sigma_{23} - \Omega_p^* \sigma_{31} - \Omega_c^* \sigma_{32}) - \Gamma_3 \sigma_{33}, \quad (\text{S40})$$

$$\dot{\sigma}_{44} = \frac{i}{2}(\Omega_d \sigma_{14} + \Omega_i \sigma_{24} - \Omega_d^* \sigma_{41} - \Omega_i^* \sigma_{42}) - \Gamma_4 \sigma_{44}, \quad (\text{S41})$$

$$\dot{\sigma}_{21} = \xi_{21} \sigma_{21} + \frac{i}{2}(\Omega_c^* \sigma_{31} + \Omega_i^* \sigma_{41} - \Omega_p \sigma_{23} - \Omega_d \sigma_{24}), \quad (\text{S42})$$

$$\dot{\sigma}_{31} = \xi_{31} \sigma_{31} + \frac{i}{2}[\Omega_p(\sigma_{11} - \sigma_{33}) + \Omega_c \sigma_{21} - \Omega_d \sigma_{34}], \quad (\text{S43})$$

$$\dot{\sigma}_{32} = \xi_{32} \sigma_{32} + \frac{i}{2}[\Omega_p \sigma_{12} + \Omega_c(\sigma_{22} - \sigma_{33}) - \Omega_i \sigma_{34}], \quad (\text{S44})$$

$$\dot{\sigma}_{41} = \xi_{41} \sigma_{41} + \frac{i}{2}[\Omega_d(\sigma_{11} - \sigma_{44}) + \Omega_i \sigma_{21} - \Omega_p \sigma_{43}], \quad (\text{S45})$$

$$\dot{\sigma}_{42} = \xi_{42} \sigma_{42} + \frac{i}{2}[\Omega_i(\sigma_{22} - \sigma_{44}) + \Omega_d \sigma_{12} - \Omega_c \sigma_{43}], \quad (\text{S46})$$

$$\dot{\sigma}_{43} = \xi_{43} \sigma_{43} + \frac{i}{2}(\Omega_d \sigma_{13} + \Omega_i \sigma_{23} - \Omega_p^* \sigma_{41} - \Omega_c^* \sigma_{42}), \quad (\text{S47})$$

$$(\text{S48})$$

where  $\xi_{21} = i(\delta_p - \delta_c) - \gamma_{21} = i\delta_2 - \gamma_{21}$ ,  $\xi_{31} = i\delta_p - \gamma_{31}$ ,  $\xi_{32} = i\delta_c - \gamma_{32}$ ,  $\xi_{41} = i\delta_d - \gamma_{41}$ ,  $\xi_{42} = i(\delta_d - \delta_2) - \gamma_{42}$ ,  $\xi_{43} = i(\delta_d - \delta_p) - \gamma_{43}$ ,  $\Gamma_3 = \Gamma_{31} + \Gamma_{32}$ ,  $\Gamma_4 = \Gamma_{41} + \Gamma_{42}$ . We consider the weak probe and idler perturbation and calculate the steady-state solution. To the zero order (i.e.  $\Omega_p = 0 = \Omega_i$ ), the solutions of the density matrix elements  $\sigma_{12}, \sigma_{13}, \sigma_{24}, \sigma_{43}$  and their transpose are zero, because there are no laser fields to create their coherences. By solving the two coherence evolution equations for  $\sigma_{32}$  and  $\sigma_{41}$  and the zero population equations, in addition to the population conservation law, one obtains the steady-state solution for the zero-order populations which are

$$\sigma_{11}^{(0)} = \frac{\frac{\Gamma_{42}}{\Gamma_{31}}(1 + \frac{2\Gamma_3|\xi_{32}|^2}{\gamma_{32}|\Omega_c|^2})}{2(1 + \frac{\Gamma_{42}}{\Gamma_{31}} + \frac{\Gamma_{42}\Gamma_3|\xi_{32}|^2}{\Gamma_{31}\gamma_{32}|\Omega_c|^2} + \frac{\Gamma_4|\xi_{41}|^2}{\gamma_{41}|\Omega_d|^2})}, \quad (\text{S49})$$

$$\sigma_{22}^{(0)} = \frac{1 + \frac{2\Gamma_4|\xi_{41}|^2}{\gamma_{41}|\Omega_d|^2}}{2(1 + \frac{\Gamma_{42}}{\Gamma_{31}} + \frac{\Gamma_{42}\Gamma_3|\xi_{32}|^2}{\Gamma_{31}\gamma_{32}|\Omega_c|^2} + \frac{\Gamma_4|\xi_{41}|^2}{\gamma_{41}|\Omega_d|^2})}, \quad (\text{S50})$$

$$\sigma_{33}^{(0)} = \frac{\frac{\Gamma_{42}}{\Gamma_{31}}}{2(1 + \frac{\Gamma_{42}}{\Gamma_{31}} + \frac{\Gamma_{42}\Gamma_3|\xi_{32}|^2}{\Gamma_{31}\gamma_{32}|\Omega_c|^2} + \frac{\Gamma_4|\xi_{41}|^2}{\gamma_{41}|\Omega_d|^2})}, \quad (\text{S51})$$

$$\sigma_{44}^{(0)} = \frac{1}{2(1 + \frac{\Gamma_{42}}{\Gamma_{31}} + \frac{\Gamma_{42}\Gamma_3|\xi_{32}|^2}{\Gamma_{31}\gamma_{32}|\Omega_c|^2} + \frac{\Gamma_4|\xi_{41}|^2}{\gamma_{41}|\Omega_d|^2})}. \quad (\text{S52})$$

$$(\text{S53})$$

Putting the zero-order solutions into the four first-order equations for the coherences,  $\sigma_{21}$ ,  $\sigma_{31}$ ,  $\sigma_{42}$ , and  $\sigma_{43}$ , one obtains the steady-state, and first-order solutions of the two coherence terms,  $\sigma_{31}$  and  $\sigma_{42}$ . The position-dependent phase factor is restored into the Rabi frequency and the relation between the atomic coherence and the slowly-varying macroscopic polarization is used, i.e.,

$$P_{p(i)} = 2n_a d_{31(42)} \sigma_{31(42)} e^{-ik_{p(i)} \cdot \vec{r}}, \quad (\text{S54})$$

where  $n_a$  is the atomic density. The slowly-varying polarizations can be written as

$$P_p = \varepsilon_0 \chi_{pp} E_p + \varepsilon_0 \chi_{pi} E_i e^{i(2\vec{k}_c - \vec{k}_i - \vec{k}_p) \cdot \vec{r}}, \quad (\text{S55})$$

$$P_i = \varepsilon_0 \chi_{ii} E_i + \varepsilon_0 \chi_{ip} E_p e^{i(2\vec{k}_c - \vec{k}_p - \vec{k}_i) \cdot \vec{r}}, \quad (\text{S56})$$

with the susceptibilities

$$\chi_{pp} = \frac{in_a |d_{31}|^2}{D \varepsilon_0 \hbar} \left\{ \frac{\xi_{43}^* \xi_{42}^* + \frac{1}{4} |\Omega_c|^2 (1 - |\epsilon|^2)}{\xi_{32}^*} \sigma_{22,33}^{(0)} - \left[ \frac{\xi_{42}^* \xi_{21} \xi_{43}^*}{|\Omega_c|^2 / 4} + (|\epsilon|^2 \xi_{43}^* + \xi_{21}) \right] \sigma_{11,33}^{(0)} + |\epsilon|^2 \frac{\xi_{21} \xi_{42}^* + \frac{1}{4} |\Omega_c|^2 (|\epsilon|^2 - 1)}{\xi_{41}^*} \sigma_{11,44}^{(0)} \right\}, \quad (\text{S57})$$

$$\chi_{pi} = \frac{in_a d_{31} d_{42} \Omega_c \Omega_d}{\varepsilon_0 \hbar |\Omega_c|^2 D} \left\{ \frac{\xi_{21} \xi_{42}^* + \frac{1}{4} |\Omega_c|^2 (|\epsilon|^2 - 1)}{\xi_{32}^*} \sigma_{22,33}^{(0)} + (\xi_{43}^* + \xi_{21}) \sigma_{22,44}^{(0)} + \frac{\xi_{43}^* \xi_{42}^*}{\xi_{41}^*} \sigma_{11,44}^{(0)} \right\}, \quad (\text{S58})$$

$$\chi_{ii} = \frac{in_a |d_{42}|^2 \xi_{31}^*}{\varepsilon_0 \hbar D} \left\{ |\epsilon|^2 \frac{4\xi_{43} \xi_{31}^* + |\Omega_c|^2 (|\epsilon|^2 - 1)}{\xi_{41}^* \xi_{31}^*} \sigma_{11,44}^{(0)} + \frac{4\xi_{21}^* \xi_{31}^* + |\Omega_c|^2 (1 - |\epsilon|^2)}{4\xi_{32}^* \xi_{31}^*} \sigma_{22,33}^{(0)} - \left[ \frac{\xi_{21}^* \xi_{43}}{|\Omega_c|^2 / 4} + \frac{\xi_{43} + \xi_{21}^* |\epsilon|^2}{\xi_{31}^*} \right] \sigma_{22,44}^{(0)} \right\}, \quad (\text{S59})$$

$$\chi_{ip} = \frac{in_a d_{31} d_{42} \xi_{31}^* \Omega_c \Omega_d}{\varepsilon_0 \hbar D |\Omega_c|^2} \left\{ \left[ \frac{\xi_{43}}{\xi_{32}^*} - \frac{|\Omega_c|^2 (1 - |\epsilon|^2)}{4\xi_{32} \xi_{31}^*} \right] \sigma_{22,33}^{(0)} + \frac{\xi_{43} + \xi_{21}^*}{\xi_{31}^*} \sigma_{11,33}^{(0)} + \left[ \frac{\xi_{21}^*}{\xi_{41}^*} - \frac{|\Omega_c|^2 (|\epsilon|^2 - 1)}{4\xi_{41} \xi_{31}^*} \right] \sigma_{11,44}^{(0)} \right\}, \quad (\text{S60})$$

$$D = \frac{\xi_{31} \xi_{42}^* \xi_{21} \xi_{43}^*}{|\Omega_c|^2 / 4} + \xi_{43}^* (\xi_{42}^* + |\epsilon|^2 \xi_{31}) + \xi_{21} (\xi_{42}^* |\epsilon|^2 + \xi_{31}) + \frac{1}{4} (|\epsilon|^2 - 1)^2, \quad (\text{S61})$$

where  $\epsilon = \Omega_d / \Omega_c$  and in the scheme of Fig. 1(b) of the main context,  $\epsilon = -\sqrt{7}$  and  $\sigma_{ii,jj}^{(0)} = \sigma_{jj}^{(0)} - \sigma_{ii}^{(0)}$  ( $i = \{1, 2\}, j = \{3, 4\}$ ) is the population difference. For the beams nearly copropagating on the  $z$ -axis, the steady-state Maxwell equations for the probe and idler fields are

$$\frac{\partial E_p}{\partial z} = \frac{ik_p}{2} \chi_{pp} E_p + \frac{ik_p}{2} \chi_{pi} e^{i\Delta k_z z} E_i^*, \quad (\text{S62})$$

$$\frac{\partial E_i}{\partial z} = \frac{ik_i}{2} \chi_{ii} E_i + \frac{ik_i}{2} \chi_{ip} e^{i\Delta k_z z} E_p^*, \quad (\text{S63})$$

where  $\Delta k_z = 2n_c \vec{k}_c - k_p \cos\theta - k_i \sin\theta$ . The index of refraction for the control field  $n_c$  is explicitly added since the control field off-resonantly drives the probe transition with the major population located in state  $|1\rangle$ . We do not consider the Maxwell equation for the control field. The index of refraction  $n_c$  is calculated from the two-level response, i.e.  $n_c = \sqrt{\chi_c} \cong 1 + \chi_c/2$  with

$$\chi_c = -\frac{n_a d_{41}^2}{\varepsilon_0 \hbar} \frac{\delta_d}{\delta_d^2 + \Gamma_4^2/4}. \quad (\text{S64})$$

The coupled Maxwell equations for the probe and idler fields can be solved to be

$$E_p = E_{p0} \exp(\delta a L) [\cosh(\xi L) + \frac{a}{\xi} \sinh(\xi L)], \quad (\text{S65})$$

$$E_i^* = E_{p0} \frac{a_{ip}}{\xi} \exp(\delta a L) \sinh(\xi L), \quad (\text{S66})$$

where  $a_{pj} = \frac{ik_p}{2} \chi_{pj}$ ,  $a_{ij} = \frac{ik_i}{2} \chi_{ij}$ ,  $j = \{i, p\}$  and  $a = (a_{ii} + a_{pp} - i\Delta k_z)/2$ ,  $\delta a = (a_{pp} - a_{ii} + i\Delta k_z)/2$ ,  $\xi = \sqrt{a^2 - a_{pi}a_{ip}}$ . The FWM probe gain can be calculated by Eq. (S65).

- 
- [S1] Y.-W. Lin, H.-C. Chou, P. P. Dwivedi, Y.-C. Chen, and I. A. Yu. Opt. Express. **16**, 3753(2008).  
[S2] L. E. Richter, H. I. Mandelberg, M. S. Kruger, and P. A. Mcgrath. IEEE J. Quant. Electron. **QE22**, 2070(1986).  
[S3] R. Schermaul, R. C. M. Learner, D. A. Newnham, R. G. Williams, J. Ballard, N. F. Zobov, D. Belmiloud, and J. Tennyson. J. Mol. Spectro. **208**, 32(2001).  
[S4] Y.-F. Chen, Y.-C. Liu, Z.-H. Hsai, S.-H. Wang, and I. A. Yu. Phys. Rev. A, **72**, 033812(2005).  
[S5] Y.-F. Chen, Y.-M. Kao, W.-H. Lin, and I. A. Yu. Phys. Rev. A **74**, 063807(2006).  
[S6] N. Lauk, C. O'Brien, and M. Fleischhauer. Phys. Rev. A, **88**, 013823(2013).  
[S7] M. T. Turnbull, P. G. Petrov, C. S. Embrey, A. M. Marino, and V. Boyer Phys. Rev. A, **88**, 033845(2013).